

<https://doi.org/10.1038/s41612-025-01215-5>

Aerosol effects on Maritime Continent precipitation: Oceanic intensification and land diurnal cycle delay



Kyong-Hwan Seo^{1,2}✉, Jinho Choi¹, Seoung Soo Lee^{3,4,5}✉, William K. M. Lau³, Tomoki Miyakawa⁶ & Han-Gyul Jin^{1,2}

Aerosols affect radiation, cloud properties, convection, air temperature, and large-scale circulation, yet their influence on precipitation distribution over the Maritime Continent (MC), a complex tropical region composed of islands interspersed with shallow seas, remains poorly understood. Using high-resolution cloud-system resolving model simulations, satellite observations, and reanalysis data, we demonstrate that rising aerosol concentrations amplify oceanic precipitation more than they suppress land precipitation, thereby increasing the sea-to-land precipitation ratio over the MC. This shift is supported by observations and contrasts with the land-enhanced precipitation distribution seen in pristine simulations or those without aerosol radiative effects. Our results underscore that aerosol-induced radiative cooling stabilizes the lower troposphere more over land than over the ocean, enhancing low-level convergence and convection over the sea. Moreover, high aerosol concentrations delay the diurnal precipitation peak over land from late afternoon to midnight, driven by diminished daytime heating and subsequent nighttime increases in moist static energy—an interesting pattern evident in some observed high-aerosol days.

Aerosols are tiny solid or liquid particles suspended in the Earth's atmosphere. These particles vary in size, composition, and origin, influencing air quality, climate, and weather patterns. Aerosols can be natural (e.g., sea salt, dust, volcanic ash, and organic compounds from vegetation) or anthropogenic (e.g., soot, sulfates, nitrates, and industrial pollutants). Aerosols affect atmospheric dynamics through both radiative and microphysical processes. Radiative effects of aerosols involve the scattering and absorption of incoming solar radiation, which alters atmospheric heating rates and surface energy fluxes, ultimately impacting atmospheric stability^{1–3}. On the other hand, aerosol microphysical effects occur when aerosols serve as cloud condensation nuclei (CCN) and ice nuclei (IN), modifying cloud microphysics, albedo, and lifetime^{4,5}. For constant water availability, these aerosols act to reduce the size of cloud droplets and to increase cloud albedo, resulting in surface cooling. In addition, the formation of smaller and lighter droplets leads to greater vertical cloud development and an extended cloud lifetime⁶. These aerosols also affect latent heat distribution and convection intensity^{1,7,8}. Absorbing aerosols, however, cause heating in a cloud layer, reducing relative humidity and leading to cloud dissipation (a phenomena known as the semi-direct effect).

These aerosol-induced modifications influence key meteorological phenomena as well as the regional and global energy budget. For example, aerosols lead to surface cooling over China, reducing the land–sea thermal contrast and subsequently weakening East Asian monsoon circulation⁹. This phenomenon has been referred to as the “north drying and south wetting” pattern over eastern China during summertime. Increased aerosol concentrations have been found to delay the formation of tropical cyclones, reduce their peak intensity, and lead to earlier dissipation¹⁰. However, an increase in precipitation is observed within the expanded rainbands of these cyclones. These findings suggest that while aerosols may weaken the central strength of tropical cyclones, they can enhance rainfall in the surrounding areas, indicating a complex role of aerosols in modulating storm behavior. Additionally, biomass-burning-produced smoke over Central America has been shown to enhance tornado genesis, intensity, and longevity¹¹. Furthermore, wildfire aerosols may induce interhemispheric temperature asymmetry through radiative and microphysical effects¹². As such, the presence of aerosols can influence cloud properties, precipitation patterns, and large-scale convective systems, ultimately affecting the regional^{13–16} and global^{17–19} climate.

¹Department of Atmospheric Sciences, Research Center for Climate Sciences, Pusan National University, Busan, Republic of Korea. ²Institute for Future Earth, Pusan National University, Busan, Republic of Korea. ³Earth System Science Interdisciplinary Center, the University of Maryland, College Park, MD, USA. ⁴Science and Technology Corporation, Moffett Field, CA, USA. ⁵Research Center for Climate Sciences, Pusan National University, Busan, Republic of Korea. ⁶Atmosphere and Ocean Research Institute, the University of Tokyo, Chiba, Japan. ✉e-mail: khseo@pusan.ac.kr; slee1247@umd.edu

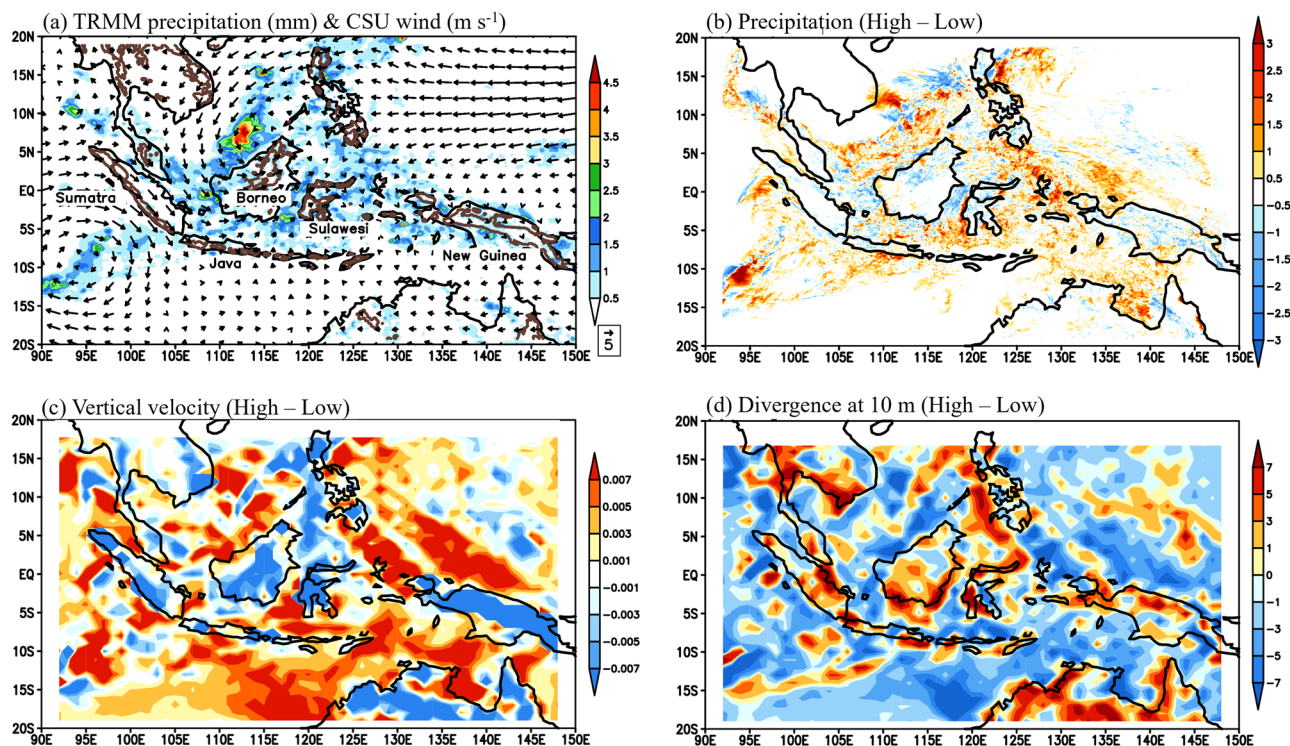


Fig. 1 | Study domain and precipitation distribution in the Maritime Continent. **a** The observed precipitation rate (TRMM3B42v7, shading, mm h^{-1}), terrain height (WRF, contours, m), and 850-hPa wind (DYNAMO CSU, arrows, m s^{-1}) averaged during simulation period (00UTC, 1st December 2011 to 00UTC, 5th December

2011). The brown solid lines (terrain height) represent only an altitude of 500 m. **b** precipitation rate (mm h^{-1}) and **c** 850-hPa vertical velocity (units of m s^{-1}), and **d**, horizontal divergence at 10 m (units of 10^{-6} s^{-1}) for high- minus low-aerosol runs.

The Maritime Continent (MC) and Southeast Asia are recognized as major sources of both biomass-burning aerosol and industrial pollution, primarily due to rapid industrialization and urbanization^{20–23}. In particular, the MC, with its complex geography of islands, coastal regions, and surrounding oceanic areas, serves as a critical region for atmospheric processes and climatic variability since this area is a region characterized by deep convection, thereby effectively modulating atmospheric circulations and precipitation through the above aerosol–cloud–radiation interactions²⁴. However, despite the recognized importance of these interactions, the exact mechanisms through which aerosols modulate cloud microphysics, atmospheric stability, and circulation over different areas of Earth’s surface (e.g., sea vs land) have been poorly understood. Motivated by this knowledge gap, the present study seeks to develop a process-level understanding of how aerosols affect clouds, precipitation, and associated circulations over both the sea and land within the MC region, employing a modeling framework supported by observational data.

Results

Precipitation in the MC: Sea vs. land

Unlike the open seas of the Indian and Pacific Oceans, the MC is a complex region composed of a cluster of islands (e.g., Sumatra, Java, Borneo, and New Guinea) interspersed with shallow seas (Fig. 1a). Most of these islands contain mountains exceeding 500 m in elevation (contours). For the aerosol-forced simulations in this study, the Weather Research and Forecasting (WRF) three-dimensional non-hydrostatic compressible model²⁵ is employed as the Cloud-System Resolving Model (CSR). This model directly resolves the deep convection at the model grid scale with a 2-km horizontal resolution. Simulations began at 00:00 UTC December 1st, 2011 and were run for 4 days until 00:00 UTC December 5th, 2011 with different aerosol concentrations. Based on the averaged PM10 concentration during the study period, the control simulation was performed using the background aerosol number concentration of 1500^{-3} ; (see Methods and

Supplementary Figs. 1 and 2). The prescribed aerosol number concentrations are fixed rather than interactive. To analyze the influence of aerosol concentration on clouds, precipitation, and associated convection and circulation, we conducted three additional simulations: the very-low-, low-, and high-aerosol runs, forced with the background aerosol concentration of 30 cm^{-3} , 300 cm^{-3} , and 3000 cm^{-3} (Supplementary Fig. 2) at each grid point and time step. Simulations, with aerosol radiative effects turned off, were also performed to obtain the sensitivity of aerosol microphysical effect to the aerosol concentrations (Methods). Assumed aerosol radiative properties are also provided in the Methods section.

A large convective envelope was present over the MC in these periods. In fact, this event is the one phase of the Madden-Julian Oscillation (MJO), which is the dominant propagating mode of intraseasonal variability in the tropics^{26,27}. The phase-4 case was selected and simulated to investigate the physical processes and associated mechanisms governing aerosol effects on convection and precipitation. The physical parameterizations (Supplementary Table 1), model configuration, case information, and experimental details (Supplementary Table 2) can be found in Methods.

Figure 1a exhibits that during this 4-day period, oceanic precipitation over the MC exceeded precipitation over land. This particular feature is the main focus of this study and its mechanism is explored in this study. A cyclonic circulation in the lower troposphere is observed southwest of Sumatra and north of Borneo (Fig. 1a), while an anticyclonic circulation appears in the upper troposphere over the same region (not shown). These circulation features are characteristic of equatorial Rossby waves with a baroclinic mode^{28,29}. Additionally, an easterly wind from the western Pacific flows toward the MC, associated with the equatorial Kelvin wave, forming an equatorial Kelvin–Rossby wave couplet as a whole²⁸. The control aerosol-forcing experiment (Supplementary Fig. 3b) successfully simulates all of the above features, with pattern correlations of 0.91 for horizontal winds and 0.70 for precipitation relative to observations.

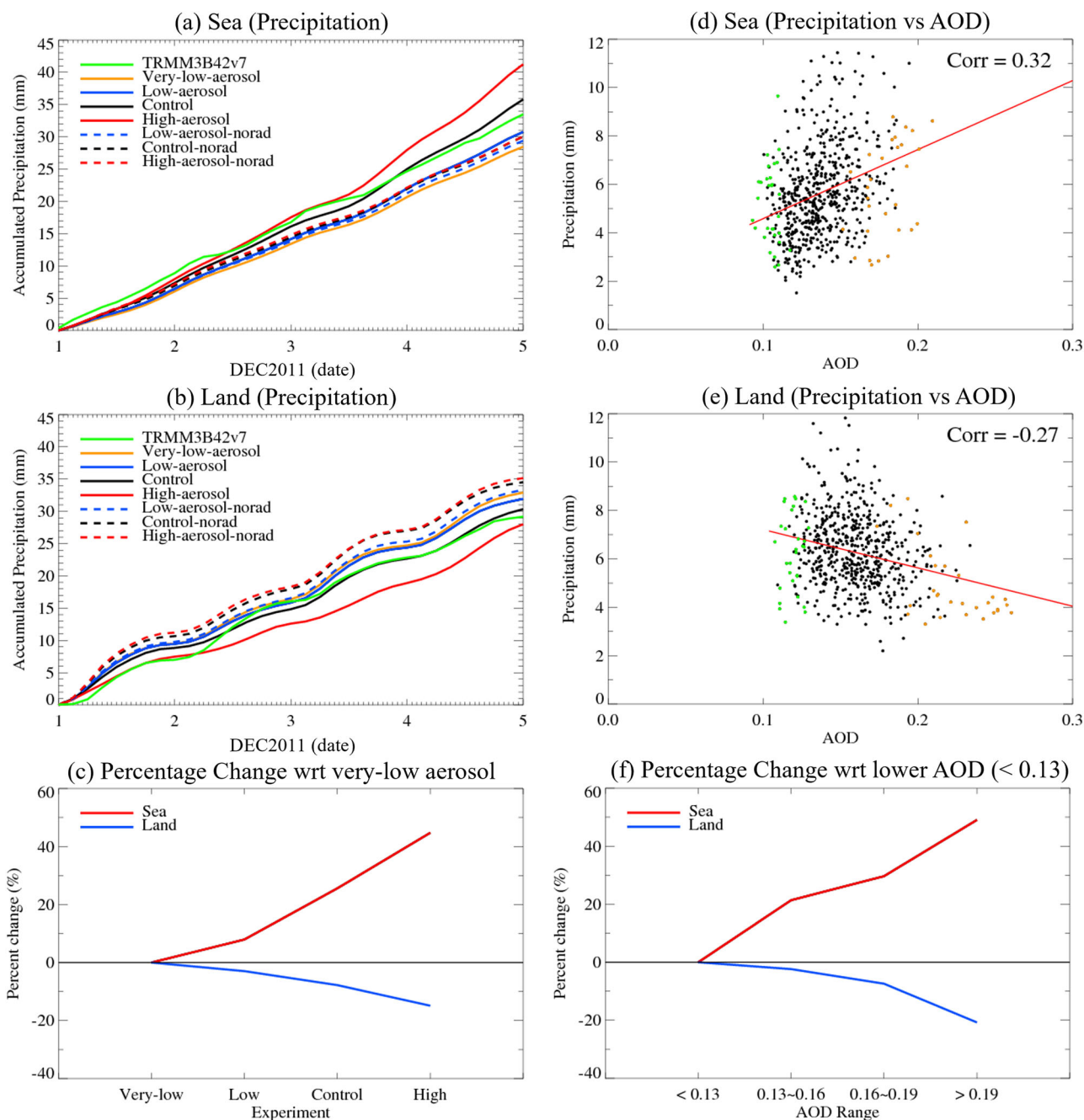


Fig. 2 | Precipitation in simulations and observations. Time series of accumulated precipitation (mm) from observations and simulations averaged over (a) sea and (b) land. The green solid line represents the TRMM3B42v7. The orange, blue, black, and red solid lines depict precipitation from the very-low-aerosol, low-aerosol, control, and high-aerosol runs, respectively, while the dashed lines represent precipitation from the low-aerosol-norad (blue), control-norad (black), and high-aerosol-norad (red) runs. Here, ‘norad’ refers to simulations without direct aerosol radiative effects. The abscissa indicates the simulation period, from December 1st to December 4th, 2011. The ordinate represents accumulated precipitation in each time step. TRMM3B42 (simulations) has a 3-hour (1-hour, respectively) temporal resolution. c Percentage change in precipitation (%) for each experiment relative to the very-

low-aerosol run over the sea (red) and land (blue). Observed daily precipitation and MERRA-2 AOD averaged separately for (d) sea and (e) land during October to February for El Niño-Southern Oscillation (ENSO)-neutral years 2001, 2003, 2012, and 2013 (i.e., El Niño and La Niña years are excluded to avoid their influence). The correlation coefficients are also shown; based on the average e-folding timescale (approximately 6 days) from the autocorrelation of the AODs, these values are significant at the 95% confidence level. The orange and green dots represent aerosol days having upper 5% and lower 5% AOD conditions (high-AOD and low-AOD, respectively). The events are used to plot Fig. 6c, d, f Observed (TRMM3B42v7) percentage change in precipitation (%) for sea (red) and land (blue) relative to very low-aerosol events (AOD values less than 0.13).

Oceanic precipitation intensification

Figure 2 presents the time series of accumulated precipitation averaged over the sea and land in the seven simulations and TRMM observations. The control run (Fig. 2a,b) effectively captures the observed evolution of precipitation, with differences between the control run and TRMM3B42v7 remaining within 10% (Table 1). The precipitation over the sea in the

control run exceeds that over land by 18%, a similar ratio observed in TRMM3B42v7, which is 15%. As aerosol concentration increases, precipitation over the sea intensifies, while it decreases over land. The very low-aerosol simulation clearly shows a land-enhanced precipitation distribution. This is primarily due to two factors: (1) land experiences stronger surface heating and more daytime convection (see Fig. 6b), and (2) the land-sea

Table 1 | Accumulated precipitation (mm) and ratio of precipitation averaged over the sea to land in the observation and each simulation. ‘norad’ refers to simulations without direct aerosol radiative effects

Observation or Experiment	Sea	Land	Ratio (Sea/Land)
TRMM	33.5	29.2	1.15
Very-low-aerosol	28.5	32.9	0.87
Low-aerosol	30.8	31.9	0.97
Control	35.8	30.3	1.18
High-aerosol	41.2	28.0	1.47
Low-aerosol-norad	29.4	33.3	0.88
Control-norad	30.0	34.5	0.87
High-aerosol-norad	30.1	35.1	0.86

thermal contrast is stronger, further enhancing moisture convergence over land. The sea-to-land precipitation ratio rises from 0.87 and 0.97 in the very-low- and low-aerosol runs to 1.47 in the high-aerosol run. The spatial pattern of precipitation for the high-minus low-aerosol runs (Fig. 1b) shows an enhancement over the ocean relative to land, a characteristic similar to that seen in the observations (Fig. 1a).

All simulations without direct aerosol radiative effects (i.e., low-aerosol-norad, control-norad, and high-aerosol-norad) yield precipitation amounts comparable to those in the full experiments, indicating a substantial role for aerosol microphysics. These also exhibit greater precipitation in land than in sea (Fig. 2a,b and Table 1). Cumulative precipitation at the final time step over land exceeds that over the sea by ~12–14% in these norad runs. This is because land heats up quickly and destabilizes more easily in the absence of aerosol radiative effects. Another interesting feature in Fig. 2a,b is that as aerosol concentration increases, the relative increase in oceanic precipitation compared to the very-low-aerosol run is greater than the relative decrease in land precipitation, as shown in Fig. 2c. The percentage precipitation change over the sea is 45–50%, which is more than twice the absolute change over land. This ocean-preferred feature also appears in the observations (Fig. 2d–f): both the statistically significant increase (decrease) in precipitation over the sea (land) (Fig. 2d, e) and the intensified sea-to-land precipitation ratio (Fig. 2f), as revealed by MERRA-2 (Modern-Era Retrospective Analysis for Research and Applications, Version 2) aerosol optical depth (AOD) and TRMM precipitation data, occur with increasing aerosol concentrations. This oceanic intensification is a new discovery, and the underlying mechanism is presented.

On the other hand, from Fig. 2a, b and Table 1, it is evident that the sensitivity of precipitation to changes in aerosol concentration is notably smaller for microphysical processes than for radiative ones. To show this, we first estimated the aerosol microphysical effect by subtracting the control-norad experiment from the high-aerosol-norad experiment and subtracting the low-aerosol-norad experiment from the control-norad experiment (Supplementary Table 3). The resulting changes are relatively minor, ranging from just 0.1 to 1.2 mm. Next, since the high-aerosol minus control and control minus low-aerosol experiments reflect both radiative and microphysical influences, the aerosol radiative effect is estimated by subtracting the above microphysical effect from the total precipitation changes (Supplementary Table 3). The absolute changes in precipitation due to the aerosol radiative effect range from 2.8 to 5.3 mm, which are much larger than those due to the aerosol microphysical effect. This suggests that microphysical response to changes in aerosol loading is much weaker compared to the radiative effect.

To understand how aerosols contribute to differences in precipitation between sea and land, we analyze time–height cross sections of static stability ($\frac{\partial \theta}{\partial z}$) differences between the high- and low-aerosol runs over the sea and land (Fig. 3a,b). Here, θ represents the potential temperature, and z denotes altitude. Firstly, over land (Fig. 3b), an increase in aerosol concentration leads to greater stability in the lower troposphere (below 800 hPa)

due to aerosol–radiation interactions, including both absorption and scattering of solar radiation. These processes reduce the amount of solar energy reaching the surface after sunrise (around 08:00 LST), leading to surface cooling (Supplementary Fig. 4c) and, consequently, increased atmospheric stability. However, after sunset (approximately 20:00 LST), stability in the lower troposphere (from the surface to 950 hPa) decreases due to surface heating (Supplementary Fig. 4d) caused by downwelling longwave radiation flux (Supplementary Fig. 7d) associated with higher aerosol concentrations, which is closely related to the diurnal cycle of the MC. This relationship will be further explored in Fig. 6.

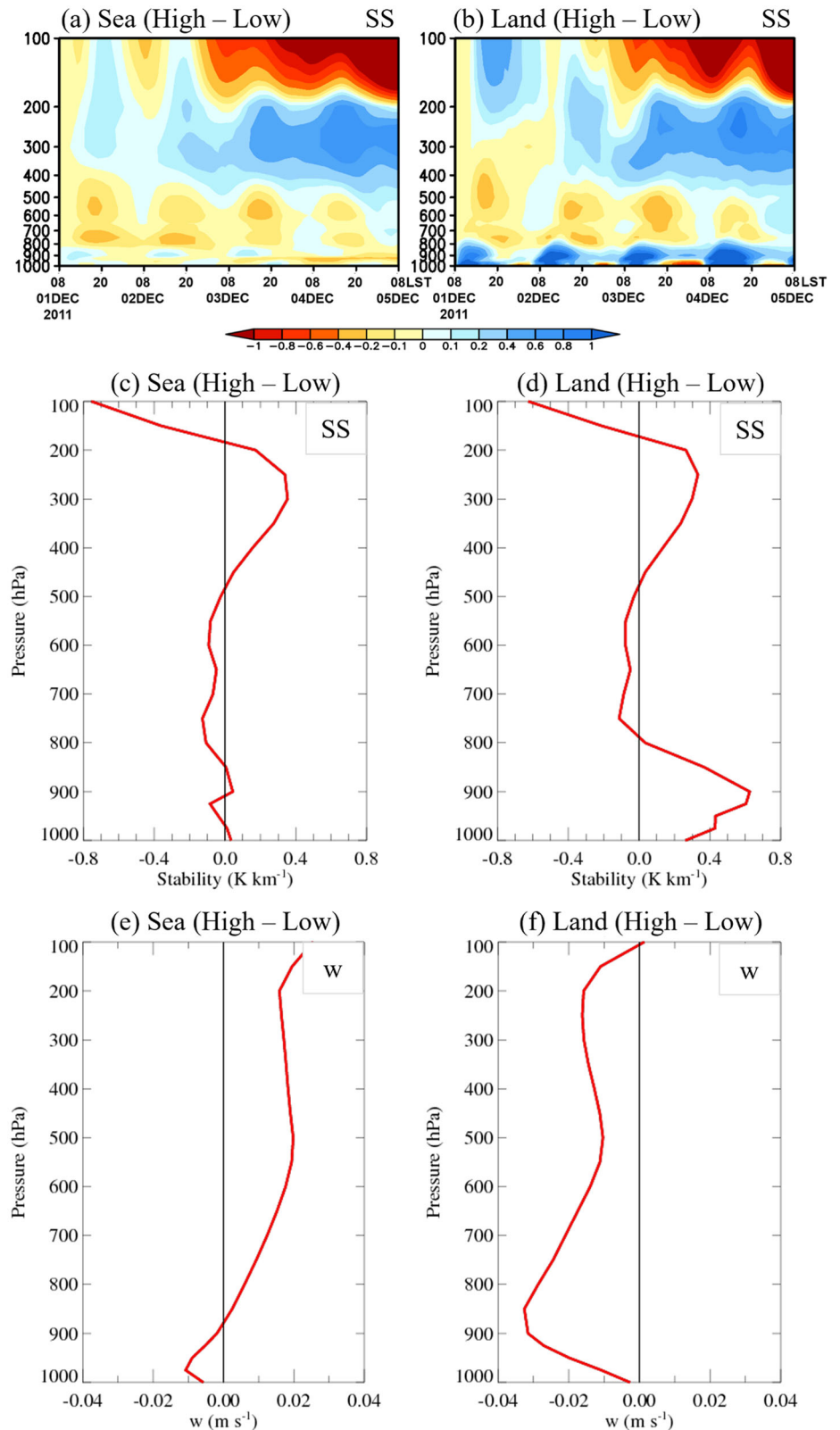
Over the sea, by contrast, changes in atmospheric stability are very weak and not demonstrably different from zero in the lower troposphere (below 800 hPa) in the high-minus-low aerosol simulations (Fig. 3a). Higher aerosol concentrations reduce the amount of solar radiation reaching the surface, causing a more pronounced temperature decrease over land. Consequently, the aerosol-induced stability changes in the lower troposphere are greater over land. Figure 3c,d present vertical profiles of stability differences between the high- and low-aerosol runs, which clearly show increased stability in the lower troposphere (surface to 800 hPa) over land. In contrast, aerosol-induced stability changes in the lower troposphere over the sea are much smaller.

To further explore the role of land–sea contrast in precipitation and atmospheric stability in response to varying aerosol concentrations, Supplementary Fig. 4a,b illustrates differences in time-averaged downward shortwave radiation at the surface and surface temperature between the high- and low-aerosol runs. Throughout the simulation period, a higher aerosol concentration reduces the amount of shortwave radiation reaching the surface over both sea and land (Supplementary Fig. 4a). This reduction induces stronger surface cooling over land due to its lower heat capacity, whereas minimal changes in surface temperature are observed over the sea (Supplementary Fig. 4b). The more significant surface cooling over land, in turn, enhances stability in the lower troposphere more strongly than over the sea (Fig. 3).

Regional and mesoscale circulations are closely linked to atmospheric stability^{30,31}. To examine how aerosol-induced changes in radiative forcing and stability influence circulations, vertical motion, a key component of circulations, is analyzed. Histograms of updraft velocity for the entire levels over the sea and land for the low-aerosol, control, and high-aerosol runs were created for this purpose (Supplementary Fig. 5). A higher frequency of updrafts across all updraft-velocity ranges is associated with increased aerosol concentrations over the sea. However, over land, the updraft frequency exhibits a negative correlation with aerosol concentration. Thus, aerosol-induced enhancements in precipitation intensity over the sea (Fig. 2a) are linked to significantly strengthened convection, which is attributed to higher heat capacity and reduced atmospheric stability compared to land. Conversely, over land (Supplementary Fig. 5b), a weaker aerosol-induced convection is evident due to poor heat retention and increased stability, leading to a reduction in precipitation (Fig. 2b,c). Vertical profiles of updraft velocity differences over the sea and land are also depicted in Fig. 3e,f. Stronger updrafts with higher aerosol concentrations occur over the sea (Fig. 3e), although higher aerosol concentrations weaken updraft velocity below 900 hPa (approximately 1 km). This weakening, however, is less pronounced over the sea than over land. In contrast, greater atmospheric stability over land (Fig. 3d and Supplementary Fig. 4) results in weaker updrafts with higher aerosol concentrations (Fig. 3f). Specifically, near the planetary boundary layer (PBL) height (approximately 1.0 to 1.5 km, 900 to 850 hPa), the aerosol-induced weakening of the ascending flow is most prominent over land. This occurs partly because differences in aerosol concentrations between the simulations are greater below the PBL top than above it.

In the spatial distribution (Fig. 1c,d), stronger aerosol-induced upward motions are evident over the sea, while weaker upward motions occur over land. The intensified upward motions over the sea correspond to enhanced low-level convergence, indicating aerosol-induced enhancements in low-level convergence drive stronger convection, increased updraft intensity, and enhanced precipitation over the sea (Fig. 2a,c). In contrast, over land

Fig. 3 | Static stability and updraft velocity over the sea and land. Time-height cross section of difference in stability ($\frac{\partial\theta}{\partial z}$, K km⁻¹) between the high- and low-aerosol runs, averaged over (a) sea and (b) land in the domain of Fig. 1a. Note that θ indicates potential temperature and z is altitude. The abscissa indicates LST. The ordinate represents pressure (hPa). Vertical profile of the difference in static stability ($\frac{\partial\theta}{\partial z}$, K km⁻¹) between the high- and low-aerosol runs, averaged over (c) sea and (d) land. **e, f**, Vertical profile of the difference in updraft velocity (m s⁻¹) between the high- and low-aerosol runs, averaged over (e) sea and (f) land.



(e.g., Sumatra, Borneo, Sulawesi, New Guinea, and northern Australia), the aerosol-induced increases in atmospheric stability (Fig. 3d) lead to low-level divergence (Fig. 1d) and downdraft anomalies (Fig. 1c), which result in the suppression of convection and precipitation (Fig. 2b,c). To confirm the aforementioned physical sequence, we calculate the lead-lag correlation between the static stability over land and upward motion or precipitation

over the sea (Fig. 4). The results show that an increase in land static stability precedes oceanic upward motion or precipitation by one hour. Therefore, changes in static stability due to aerosol radiative effect is a main cause of this differential precipitation pattern between the sea and land. The above causal relationships and physical processes leading to enhanced oceanic precipitation (Fig. 2c) compared to land can be further substantiated by

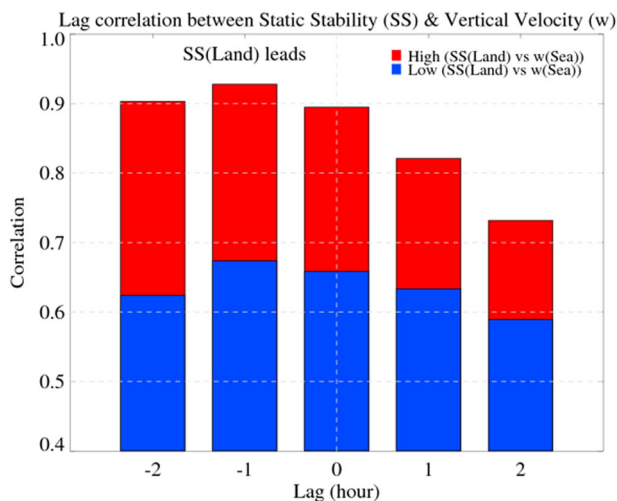


Fig. 4 | Temporal relationship between static stability and updraft velocity. Lead-lag correlation between static stability over land and updraft velocity over sea at 900 hPa for the high-aerosol minus control (red) and low-aerosol minus control (blue) simulations. Notice that the maxima appear at lag -1 hour. Note that the correlation between updraft velocity over the sea and precipitation over the sea is maximized at lag 0.

examining the percentage changes in static stability, updraft velocity, and specific humidity in the high-aerosol simulation relative to the very-low-aerosol run over both sea and land (Fig. 5), as was done in Fig. 2c. A much stronger thermodynamic response is found over land—namely, a threefold increase in static stability compared to the sea—resulting in a marked suppression of updraft velocity and precipitation. In contrast, over the sea, enhanced lower-level instability induces stronger updrafts, which, together with abundant moisture, result in increased precipitation.

Delayed diurnal cycle peak in land

Aerosol radiative effects regulate the diurnal cycle over the MC differently for the sea and land. Figure 6a,b presents the diurnal cycle of mean precipitation rates over both sea and land from observations (TRMM3B42v7) and simulations. The overall evolution of precipitation in the control run closely aligns with observations, albeit with slightly higher precipitation rates near the peak time. During the daytime over land, strong solar radiation increases instability, enhancing convection and precipitation, with peak activity occurring between 16:00 and 18:00 LST in the control run. Over the sea, however, precipitation primarily develops at night, peaking between 02:00 and 05:00 LST in the control run. This nighttime and early morning peak over the sea is attributed to various factors, including strong radiative cooling in the free atmosphere, convergence due to land–sea breeze circulation³², and off-shore gravity wave propagation³³, which collectively enhance convection and rainfall during the pre-dawn hours.

As aerosol concentrations increase, the peak amplitude of the diurnal precipitation cycle over the sea intensifies (red line in Fig. 6a). However, in simulations that exclude aerosol radiative effects, changes in aerosol concentration result in negligible alterations to the diurnal cycle of precipitation. On the other hand, over land, the amplitude and peak of the diurnal precipitation cycle decrease as aerosol concentrations increase (red line in Fig. 6b). This property is closely linked to the diurnal cycle of surface temperature over land (Supplementary Fig. 6). Increased aerosol concentrations lead to reduced fluxes of solar radiation at the surface and lower surface temperatures during the daytime. This enhanced surface cooling strengthens lower tropospheric stability, leading to weaker convection and a reduced diurnal precipitation cycle. Despite a slight increase in daytime land precipitation with rising aerosol concentrations in simulations without aerosol radiative effects, the sensitivity of the diurnal precipitation cycle to aerosol concentrations is significantly smaller (Fig. 6b). These results

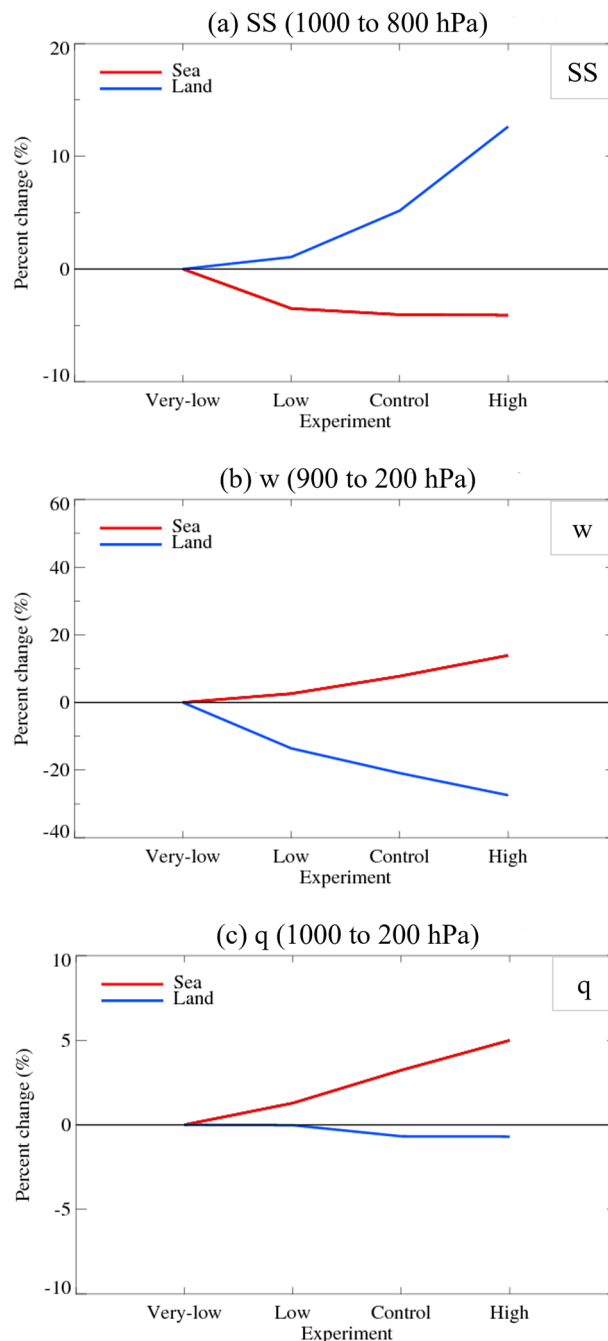
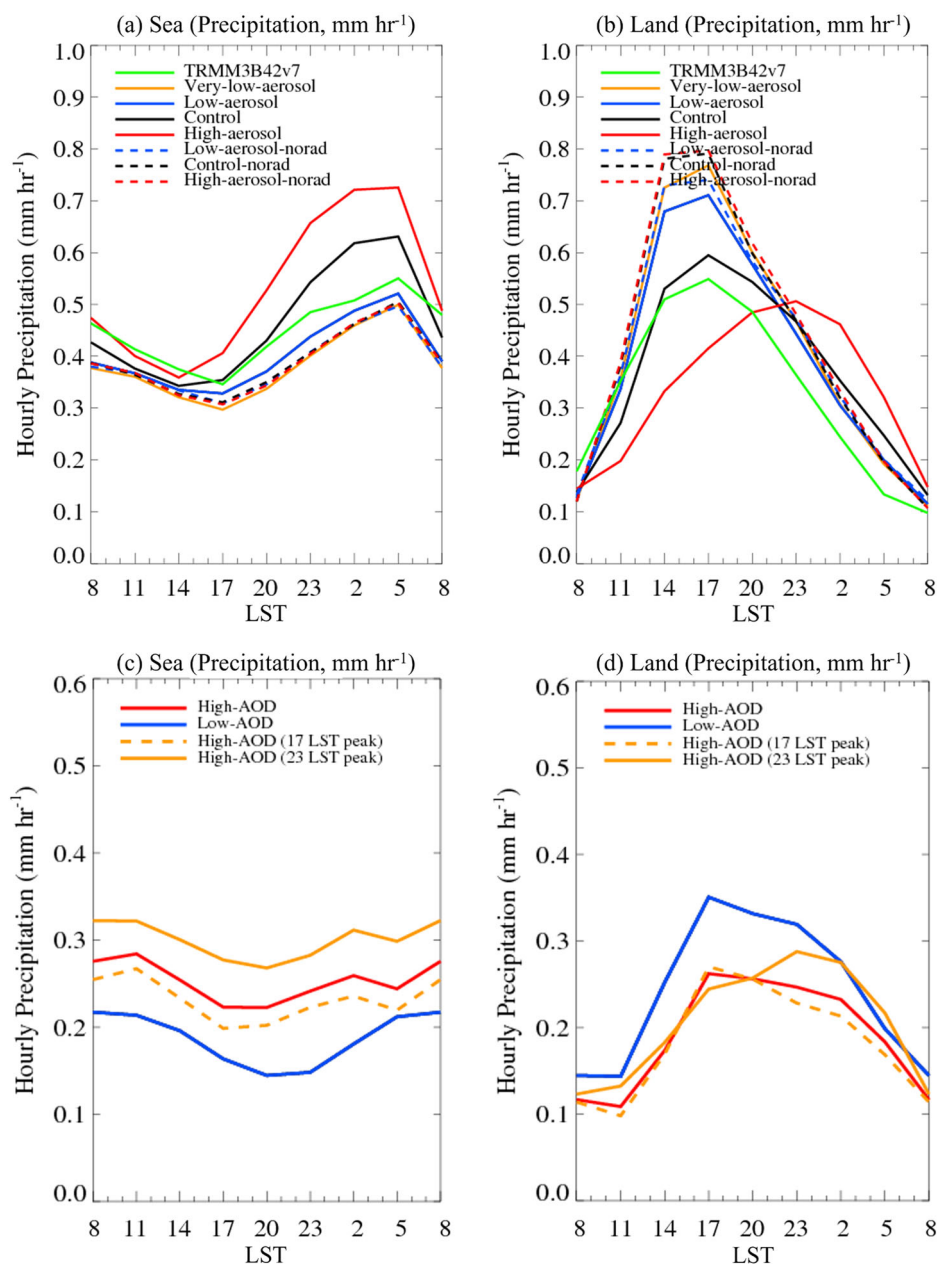


Fig. 5 | Changes in thermodynamic and dynamic variables associated with enhanced oceanic precipitation. Percentage changes (%) in (a) static stability, (b) updraft velocity, and (c) specific humidity for each experiment relative to the very-low-aerosol run over the sea (red) and land (blue), as done in Fig. 2c. The vertical levels over which each variable is averaged are indicated in the panel titles.

underscore that, in response to variations in aerosol loadings, radiative effects exert a stronger influence than microphysical effects over the MC.

Interestingly, the peak time of the diurnal cycle of precipitation over land shifts from late afternoon (17:00 LST) in the control or low-aerosol run to midnight (23:00 LST) in the high-aerosol run as aerosol concentrations increase (Fig. 6b). To identify the cause of this shift, differences in the diurnal cycle of moist static energy (MSE) at 900 hPa between the high- and low-aerosol runs are shown in Supplementary Fig. 7. Note that 900 hPa is where differences in stability and updraft velocity over land are maximized between simulations, as shown in Fig. 3d,f. MSE in the high-aerosol run is lower than in the low-aerosol run during daytime; as described before, lower

Fig. 6 | Diurnal cycle of precipitation over the sea and land. Mean diurnal cycle of the precipitation rate (mm hr^{-1}) from observations and simulations, averaged over (a) sea and (b) land. The green solid line represents TRMM precipitation. The orange, blue, black, and red solid lines indicate precipitation from the very-low-aerosol, low-aerosol, control, and high-aerosol runs, respectively, while the dashed lines represent precipitation from the low-aerosol-norad (blue), control-norad (black), and high-aerosol-norad (red) runs. ‘norad’ denotes simulations in which direct aerosol radiative effects are excluded. The abscissa denotes local standard time (LST), corresponding to UTC + 8 h. Mean diurnal cycle of the TRMM precipitation rate (mm hr^{-1}); for different levels of MERRA-2 AOD over (c) sea and (d) land during October to January in the ENSO-neutral years 2001, 2003, 2012, and 2013. The diurnal cycles for high- and low-AOD conditions (corresponding to upper 5% and lower 5% AOD days, respectively) are represented by red and blue lines, respectively. Among the high-AOD cases, two different subsets with peaks at ~17:00 LST and ~23:00 LST are also shown as dotted and solid orange lines. Their respective AOD means are nearly the same, with the former comprising two-thirds of the population and the latter one-third. Notably, for high-AOD cases, the 23:00 LST peak coexists with the conventional 17:00 LST peak.



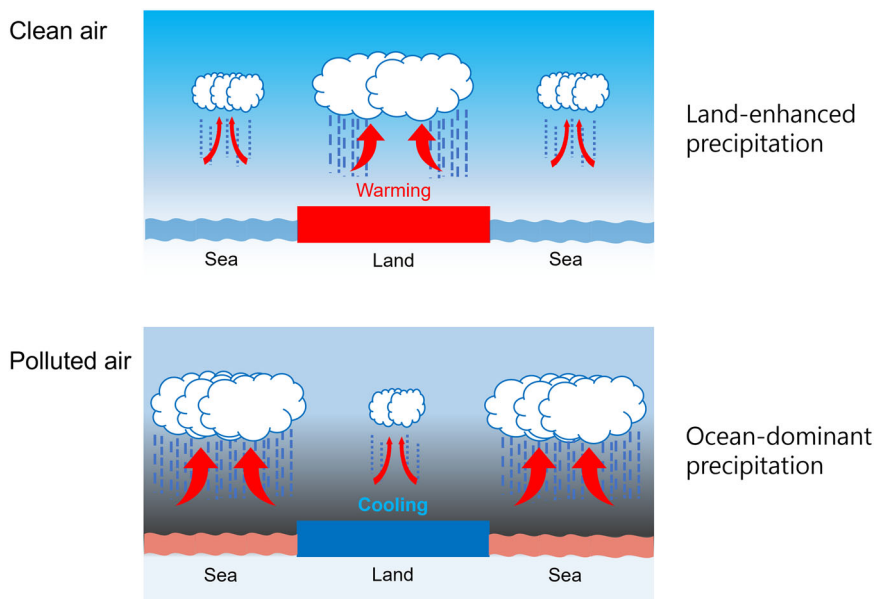
MSE over land during 08:00–16:00 LST (Supplementary Fig. 7a) is associated with greater stability (Fig. 3d) and suppressed convection (Fig. 3f) in the high-aerosol run compared to the low-aerosol run. At 17:00 LST, MSE begins to exceed that of the low-aerosol run, and this enhancement persists until sunrise (approximately 08:00 LST).

MSE is the sum of dry static energy (DSE) and latent static energy (LSE), and high minus low simulation results for these two components (Supplementary Fig. 7b,c) indicate similar contributions after 15 LST, with LSE slightly greater than DSE. The negative DSE and LSE during the daytime result from surface cooling (Supplementary Figs. 6 and 4c) and subsequently weakened sensible and latent heat fluxes (not shown). However, after 17:00 LST, positive differences in both DSE and LSE (and consequently in MSE, as shown in Supplementary Fig. 7a) emerge between the high- and low-aerosol simulations. The former is primarily attributed to enhanced downwelling longwave radiation (Supplementary Fig. 7d), resulting from increased atmospheric warming (Supplementary Fig. 8a) caused by greater shortwave absorption by aerosols near and above the top of the PBL in the high-aerosol case, rather than by cloud effects (Supplementary Fig. 8b,

which shows negative cloud influence). The latter (i.e., LSE) results from enhanced horizontal moisture advection toward inland areas due to higher specific humidity over a more unstable sea environment in high-minus low-aerosol simulations. The enhanced specific humidity (Supplementary Fig. 7e) is the main contributor compared to changes in wind vectors (not shown). Note that the temporal evolution of convective available potential energy (CAPE) and convective inhibition (CIN) (Supplementary Fig. 9) also provides a hint for the midnight peak, with CAPE accumulating until 21:00 LST and subsequently being consumed, along with the suppression of convection by positive CIN up to 20:00 LST.

Given the prevalence of mountains in the MC, larger values of MSE are advected toward inland mountainous regions during nighttime via prevailing winds (i.e., westerly wind in the lower troposphere, as shown in Fig. 1a and Supplementary Fig. 3). As a result of subsequent orographic uplift, more precipitation occurs at night than during the day over land. These findings are consistent with the concept of ‘aerosol-enhanced conditional instability’ described by a previous study³⁴. While they focused on extreme weather events in July 2013 in southwest China, their concept may also be

Fig. 7 | Schematic diagram of precipitation inhomogeneity over the sea and land in the MC. Convection and precipitation distributions in clean (upper panel) and polluted (lower panel) environments are shown. Arrow thickness represents the strength of convection. The ocean color is shown relative to the temperature of the land. The schematic illustrates a land-enhanced precipitation regime in a clean air environment and an ocean-dominant precipitation regime in a polluted air environment. Aerosol-induced radiative cooling stabilizes the lower troposphere more over land than over the ocean, enhancing low-level convergence and convection over the sea.



applicable to tropical meteorology. In both cases, aerosol-induced stabilization during the day allows energy to build up, which is later released under favorable conditions, such as moisture advection or orographic forcing during the night. This delayed release of instability contributes to the nocturnal enhancement of precipitation over land in the MC.

Interestingly, this unexpected delay in the peak of the diurnal cycle does appear in some observed cases (Fig. 6d); a late night (23:00 LST) precipitation peak coexists with the conventional late-afternoon (17:00 LST) peak in the upper 5% of aerosol concentration events, lending observational support to the simulated shift in the diurnal precipitation cycle. This feature may be useful for weather forecasting in this region.

Discussion

In summary, our model simulation demonstrates that as aerosol concentrations rise from very low to higher levels, the precipitation distribution shifts from a land-enhanced to an ocean-dominant pattern. More importantly, the increase in oceanic precipitation is proportionally greater than the reduction in land precipitation in the MC region, a feature confirmed by observations. These results are schematically presented in Fig. 7. This oceanic precipitation enhancement is due to aerosol-induced radiative effects, which stabilize the atmosphere more over land than over the sea. Stronger low-level convergence and updrafts over the sea, driven by the ocean's lower surface sensitivity to radiative forcing and reduced atmospheric stability compared to land, and the presence of abundant moisture, contribute to enhanced precipitation. In simulations without aerosol radiative effects, land-dominant precipitation distribution persists. This is primarily due to stronger surface heating over land, which leads to more intense daytime convection, as well as the greater land–sea thermal contrast, which enhances moisture convergence over land. It is worth noting that, globally, increased aerosol loading generally leads to reduced incoming solar radiation and a net suppression of precipitation, which contrasts with the regionally enhanced oceanic precipitation observed in this study over the MC^{17,35,36}.

To partially test the robustness of the main results, three additional experiments were conducted for an opposite MJO phase (i.e., the 2011 phase 8 case) and a different year (i.e., the 2018 phase 4 and phase 8 cases). All these cases (not shown) clearly exhibited enhanced oceanic precipitation relative to land and a landward delay in the diurnal precipitation peak toward midnight, suggesting that the proposed mechanism is generally applicable to the Maritime Continent environment. A more comprehensive analysis using a larger ensemble of MJO phases, seasons, and years is planned for

future work. This study also identifies a shift in the diurnal peak of precipitation over land from the late afternoon (17:00 LST) to midnight (23:00 LST) under high aerosol concentrations. This shift is linked to aerosol-induced changes in MSE and delayed convective initiation due to reduced daytime surface heating. This interesting feature also appears in several observed high-aerosol events, suggesting that the simulation captures a realistic phenomenon with potential implications for weather forecasting.

Aerosol-induced shifts in convection and precipitation over the MC have implications for MJO propagation. Previous studies^{37,38} suggest that the diurnal cycle over the MC plays a crucial role in controlling MJO propagation, as it determines whether deep convection develops over the sea or remains confined to land. A strong diurnal cycle over land can suppress fully developed convection over the sea, thereby disrupting successful MJO propagation across the MC. Conversely, a weakened diurnal cycle over land can favor oceanic convection and facilitate MJO propagation. In line with this, the present study suggests that aerosol radiative effects, which weaken the diurnal convection cycle over land, may help promote MJO propagation across the MC by reducing convective suppression over the ocean. In relation to this, a series of longer simulations will be needed in future studies to fully uncover the underlying physical processes. In addition, further investigation into the relative importance of aerosol-induced reductions in surface radiative flux (leading to decreased destabilization) versus enhanced lower-tropospheric radiative heating (leading to increased stabilization) may provide deeper insight into the mechanisms underlying this differential precipitation response.

The present study has several implications for climate modeling and regional weather forecasting. Regarding the former, current climate models may underestimate aerosol-induced precipitation shifts in tropical regions³⁹. Improving aerosol-cloud interaction parameterizations is necessary for more accurate weather and climate predictions^{40,41}. Regarding the latter, this study provides insights into how pollution and biomass-burning aerosols impact regional precipitation^{42,43}, which is relevant for forecasting extreme weather events. Understanding aerosol effects on the MJO and monsoon systems is crucial for improving seasonal forecasts. Lastly, changes in precipitation patterns over the MC could affect water resources, agriculture, and flood risk management. Understanding aerosol influences on the hydrological cycle can help policymakers develop strategies to mitigate climate-related impacts. Lastly, although cloud microphysical processes are also important, we focused on aerosol–radiation–circulation interactions in this study. The detailed structure and evolution of the condensation rate, deposition rate, freezing rates, and mass densities of cloud liquid, rain, snow,

and hail, along with cloud cover, effective cloud size, and other related factors, will be reported elsewhere.

Methods

CSRM

The Weather Research and Forecasting (WRF) three-dimensional non-hydrostatic compressible model²⁵ is employed as the CSRM in this study. This model is well-suited for our purposes due to its capability to simulate interactions among aerosol, cloud, radiation, and circulation and thus to properly represent the aerosol's direct, indirect, and semi-direct effects mentioned in the Introduction, as well as the potential invigoration of convection accordingly. The Rapid Radiative Transfer Model for GCMs (RRTMG) shortwave and longwave radiation schemes^{44,45} are used to represent radiative processes, including the reflection, scattering, and absorption of radiation by aerosols.

In order to describe microphysical processes and associated aerosol microphysical effects, the cloud-resolving model incorporates a double-moment bulk scheme^{46–48}. This scheme predicts the mass mixing ratios and number concentrations of five hydrometeor species: cloud droplets, cloud ice, rain, snow, and graupel. A gamma distribution with fixed breadth is assumed for the size distribution of these hydrometeor species. Detailed descriptions of this bulk microphysics scheme can be found in their papers^{46–48}. The effective sizes of hydrometeors are calculated in the bulk scheme and transferred to the radiation scheme (RRTMG) to consider the impacts of clouds on radiation.

Additional physical parameterizations used in the CSRM include the Yonsei University (YSU) planetary boundary layer scheme⁴⁹, the five-layer thermal diffusion land surface scheme⁵⁰, the Monin–Obukhov surface-layer scheme⁵¹, and the single-layer urban canopy model⁵². The summary of the model physical schemes used is presented in Supplementary Table 1.

Topography and land surface are represented using high-resolution static data and the slab land surface model (LSM, Supplementary Table 1). Topography is obtained from a static geographical dataset (e.g., USGS data) during the WRF Pre-processing System stage and interpolated to the model grid. This LSM primarily simulates soil heat diffusion and assumes constant surface emissivity for upward longwave flux to enhance computational simplicity.

Case description

This study investigates the effects of aerosols on precipitation over the sea and land in the MC and explores the underlying physical mechanisms. A large convective envelope, corresponding to the MJO event of November 2011, moved near the MC in early December 2011 (Fig. 1). This event was observed during the Atmospheric Radiation Measurement (ARM) MJO Investigation Experiment/Dynamics of the MJO (AMIE/DYNAMO) field campaign^{53,54}. The event was also identified by the real-time multivariate MJO (RMM) index⁵⁵, which tracks the MJO phase and equivalent location. From December 1st to 4th, 2011, the MJO envelope was situated over the MC, corresponding to phase 4 (retrieved from <http://www.bom.gov.au/climate/mjo/graphics/rmm.74toRealtime.txt>). This case was selected and simulated to investigate the physical processes and associated mechanisms governing aerosol effects on convection and precipitation.

Dataset

To characterize the observed atmospheric conditions over the MC during the selected period, we utilized three-hourly precipitation estimates from the Tropical Rainfall Measuring Mission (TRMM) 3B42 version 7 (TRMM3B42v7)⁵⁶ and version 3b of the DYNAMO gridded wind products from the Colorado State University (CSU) Mesoscale Dynamics Group (DYNAMO CSU)^{57,58}. TRMM3B42v7, which features a three-hourly temporal resolution and a $0.25^\circ \times 0.25^\circ$ spatial resolution, is derived from a combination of microwave measurements obtained from multiple low-Earth-orbiting satellites and infrared precipitation estimates from geostationary satellites. DYNAMO CSU merges observational soundings with the European Centre for Medium-Range Weather Forecasts (ECMWF)

operational analysis, offering a three-hourly time scale, a spatial resolution of $1^\circ \times 1^\circ$, and a vertical resolution of 25 hPa. These datasets provide an observational basis for evaluating the model simulations.

We use AOD data from the MERRA-2 reanalysis, produced by NASA's GMAO. MERRA-2 AOD is constrained by multiple satellite observations, including MODIS, MISR, and AVHRR, and is available at a resolution of $0.5^\circ \times 0.625^\circ$. As it assimilates satellite retrievals, the data are observationally constrained and suitable for evaluating aerosol distributions over the Maritime Continent. However, uncertainties in satellite-based retrievals—such as cloud contamination and surface reflectance—may affect the accuracy of the reanalysis.

Simulation design

As seen in Fig. 1a, the modeling domain for this study covers the MC region (20°S to 20°N , 90° to 150°E). Simulations adopt 2-km horizontal grid spacing (3173×2158 grid dimensions) and 30 vertical levels with the top at about 18 km (average vertical resolution of 600 m). The National Centers for Environmental Prediction's Global Forecast System (GFS) final analysis data are fed to simulations for initial, lateral, and boundary conditions and updated every 6 hours. Simulations start at 00 UTC 1st December 2011 and run for 4 days until 00 UTC 5th December 2011. According to AERONET measurements⁵⁹ for the aforementioned period and domain, aerosols are, on average, an internal mixture consisting of 62% ammonium sulfate, 29% organic compounds, and 9% black carbon by mass. Aerosol particles act as either CCN or IN. Using this assumed mixture, the associated densities, the ambient relative humidity, and the radiative and activation characteristics of aerosol particles are calculated. In practice, aerosol hygroscopic growth and optical properties (e.g., extinction efficiency, single scattering albedo, and the asymmetry parameter) are precomputed offline based on a prescribed size distribution, chemical composition, and a unit concentration (1 mg^{-3} , equivalent to 1 cm^{-3} at 1 kg m^{-3} air density). These values are stored in a lookup table to enhance computational efficiency. During model integration, the aerosol number concentration and relative humidity at each grid point are used to retrieve the corresponding optical properties from the table. To produce background aerosol number concentration over the MC region, a particulate matter with a diameter less than $10 \mu\text{m}$ (PM10) was converted to aerosol number concentration based on a method similar to that in a previous study⁶⁰. During this period (from December 1st to 4th), PM10 concentration is about $30 \mu\text{g m}^{-3}$ (Supplementary Fig. 1), which is averaged from four stations in Peninsular Malaysia and Malaysian Borneo (i.e., Shah Alam, Jerantut, Kuching, and Kota Kinabalu). This PM10 concentration of $30 \mu\text{g m}^{-3}$ is converted to an aerosol number concentration of 1500 cm^{-3} based on the AERONET-measured aerosol composition and size distribution, averaged over the modeling domain. The control run is performed using this uniform aerosol number concentration across the spatial domain, and it reasonably simulates the precipitation distribution over the MC.

The aerosol number concentration is assumed to be constant in the PBL and decreases exponentially with height above it (Supplementary Fig. 2). This assumption follows the general patterns of aerosol vertical distributions⁶¹. The ratio of precipitation over the sea to that over land in the control run closely matches the observed ratio in TRMM3B42v7. To analyze the influence of aerosols on precipitation and convection, three additional simulations were performed (Supplementary Fig. 2, Supplementary Table 2). The first simulation, referred to as the very low-aerosol run (so this is a clean run), involved the background aerosol concentration to be 30 cm^{-3} at each grid point and time step. The second simulation, referred to as the low-aerosol run, involved reducing the background aerosol concentration at each grid point and time step by a factor of five. The third simulation, called the high-aerosol run, increased the background aerosol concentration by a factor of two. Additionally, to isolate the impacts of aerosol radiative effects from microphysical effects, we repeated some of these simulations with aerosol radiative effects turned off. These simulations are labeled control-norad, low-aerosol-norad, and high-aerosol-norad (Supplementary Table 2).

Data availability

All the datasets used in this study are publicly available. The Tropical Rainfall Measuring Mission (TRMM) 3B42v7 3-hourly precipitation data were obtained from NASA's Precipitation Processing System (https://disc.gsfc.nasa.gov/datasets/TRMM_3B42_7/summary). The Modern-Era Retrospective analysis for Research and Applications, Version 2 (MERRA-2) reanalysis data were accessed from the NASA GES DISC archive (<https://disc.gsfc.nasa.gov/datasets?project=MERRA-2>). Observational data from the Dynamics of the Madden-Julian Oscillation (DYNAMO) field campaign were obtained from the Colorado State University Atmospheric Science data archive (https://data.eol.ucar.edu/cgi-bin/codiac/fgr_form/id=347.240). The Weather Research and Forecasting (WRF) model version 3.3.1 source code was downloaded from the NCAR Mesoscale and Microscale Meteorology (MMM) Laboratory (https://www2.mmm.ucar.edu/wrf/users/download/get_source.html), and the Final (FNL) operational global analysis data used for model initialization were provided by the NCAR Research Data Archive (<https://rda.ucar.edu/datasets/ds083.2/>).

Code availability

Any codes used in the manuscript are available upon request from khseo@pusan.ac.kr.

Received: 7 May 2025; Accepted: 23 August 2025;

Published online: 25 September 2025

References

- Feingold, G., Jiang, H. & Harrington, J. Y. On smoke suppression of clouds in Amazonia. *Geophys. Res. Lett.* **32**, L02804 (2005).
- Li, Z., Lee, K.-H., Xin, J., Wang, Y. & Hao, W.-M. First observation-based estimates of aerosol radiative forcing at the top, bottom and inside of the atmosphere. *J. Geophys. Res.* **115**, D00K18 (2010).
- Li, J. et al. Scattering and absorbing aerosols in the climate system. *Nat. Rev. Earth Environ.* **3**, 363–379 (2022).
- Twomey, S. A., Piepgrass, M. & Wolfe, T. L. An assessment of the impact of pollution on global cloud albedo. *Tellus B* **36**, 356–366 (1984).
- Albrecht, B. A. Aerosols, cloud microphysics, and fractional cloudiness. *Science* **245**, 1227–1230 (1989).
- Abbott, T. H. & Cronin, T. W. Aerosol invigoration of atmospheric convection through increases in humidity. *Science* **371**, 83–85 (2021).
- van den Heever, S. C., Stephens, G. L. & Wood, N. B. Aerosol indirect effects on tropical convection characteristics under conditions of radiative-convective equilibrium. *J. Atmos. Sci.* **68**, 699–718 (2011).
- Beydoun, H. & Hoose, C. Aerosol-cloud-precipitation interactions in the context of convective self-aggregation. *J. Adv. Model. Earth Syst.* **11**, 1066–1087 (2019).
- Ye, J., Li, W., Li, L. & Zhang, F. “North drying and south wetting” summer precipitation trend over China and its potential linkage with aerosol loading. *Atmos. Res.* **125–126**, 12–19 (2013).
- Wang, Y., Lee, K.-H., Lin, Y., Levy, M. & Zhang, R. Distinct effects of anthropogenic aerosols on tropical cyclones. *Nat. Clim. Change* **4**, 368–373 (2014).
- Saide, P. E. et al. Central American biomass burning smoke can increase tornado severity in the U.S. *Geophys. Res. Lett.* **42**, 956–965 (2015).
- Jiang, Y. et al. Impacts of wildfire aerosols on global energy budget and climate: The role of climate feedbacks. *J. Clim.* **33**, 3351–3366 (2020).
- Bollasina, M. A., Ming, Y. & Ramaswamy, V. Anthropogenic aerosols and the weakening of the south Asian summer monsoon. *Science* **334**, 502–505 (2011).
- Li, Z. et al. Aerosol and monsoon climate interactions over Asia. *Rev. Geophys.* **54**, 866–929 (2016).
- Feng, J. et al. Aerosol impacts on regional climate: chaotic or physical effect? Preprint at *EGUsphere* <https://doi.org/10.5194/egusphere-2024-4037> (2025).
- Lee, S. S. et al. Aerosols in Southeast Asia disrupt the Hadley circulation: A rapid response perspective. *Nat. Commun.* in revision (2025).
- Ramanathan, V., Crutzen, P. J., Kiehl, J. T. & Rosenfeld, D. Aerosols, climate, and the hydrological cycle. *Science* **294**, 2119–2124 (2001).
- Intergovernmental Panel on Climate Change (IPCC) (Ed.): Clouds and Aerosols, in: Climate Change 2013 – The Physical Science Basis: Working Group I Contribution to the Fifth Assessment Report of the Intergovernmental Panel on Climate Change. Cambridge University Press, Cambridge, 571–658 (2014).
- Bellouin, N. et al. Bounding global aerosol radiative forcing of climate change. *Rev. Geophys.* **58**, e2019RG000660 (2020).
- Reid, J. S. et al. Multi-scale meteorological conceptual analysis of observed active fire hotspot activity and smoke optical depth in the Maritime Continent. *Atmos. Chem. Phys.* **12**, 2117–2147 (2012).
- Salinas, S. V. et al. Physical and optical characteristics of the October 2010 haze event over Singapore: A photometric and lidar analysis. *Atmos. Res.* **122**, 555–570 (2013).
- Nguyen, G. T. H., Shimadera, H., Uranishi, K., Matsuo, T. & Kondo, A. Numerical assessment of PM_{2.5} and O₃ air quality in Continental Southeast Asia: Impacts of future projected anthropogenic emission change and its impacts in combination with potential future climate change impacts. *Atmos. Environ.* **226**, 117398 (2020).
- Wen, T. Y. et al. Overview of aerosol and air pollution in South Eastern Asia countries. *Aerosol Air Qual. Res.* **23**, 1–30 (2023).
- Yoneyama, K. & Zhang, C. Years of the Maritime Continent. *Geophys. Res. Lett.* **47**, e2020GL087182 (2020).
- Skamarock, W. C. et al. A description of the Advanced Research WRF version 3. NCAR Tech. Note NCAR/TN-475+STR, 125 (2008).
- Madden, R. & Julian, P. Observations of the 40–50-day tropical oscillation—a review. *Mon. Weather Rev.* **122**, 813–837 (1994).
- Seo, K.-H., Lee, H.-J. & Frierson, D. M. W. Unraveling the teleconnection mechanisms that induce wintertime temperature anomalies over the Northern Hemisphere continents in response to the Madden-Julian Oscillation. *J. Atmos. Sci.* **73**, 3557–3571 (2016).
- Rui, H. & Wang, B. Development characteristics and dynamic structure of tropical intraseasonal convection anomalies. *J. Atmos. Sci.* **47**, 357–379 (1990).
- Seo, K.-H. & Son, S.-W. The global atmospheric circulation response to tropical diabatic heating associated with the Madden-Julian oscillation during Northern winter. *J. Atmos. Sci.* **69**, 79–96 (2012).
- Barthelmie, R. J. The effects of atmospheric stability on coastal wind climates. *Meteorol. Appl.* **6**, 39–47 (1999).
- Lee, S. S. Effect of aerosol on circulations and precipitation in deep convective clouds. *J. Atmos. Sci.* **69**, 1957–1974 (2012).
- Mori, S. Diurnal land–sea rainfall peak migration over Sumatera Island, Indonesian Maritime Continent, observed by TRMM satellite and intensive rawinsonde soundings. *Mon. Wea. Rev.* **132**, 2021–2039 (2004).
- Love, B. S., Matthews, A. J. & Lister, G. M. S. The diurnal cycle of precipitation over the Maritime Continent in a high-resolution atmospheric model. *Quart. J. Roy. Meteor. Soc.* **137**, 934–947 (2011).
- Fan, J. et al. Substantial contribution of anthropogenic air pollution to catastrophic floods in Southwest China. *Geophys. Res. Lett.* **42**, 6066–6075 (2015).
- Rosenfeld, D. et al. Flood or drought: How do aerosols affect precipitation?. *Science* **321**, 1309–1313 (2008).
- Guo et al. Declining global atmospheric moisture and precipitation trends due to aerosols. *Nat. Geosci.* **9**, 870–874 (2016).
- Hagos, S. M. et al. The impact of the diurnal cycle on the propagation of Madden-Julian Oscillation convection across the Maritime Continent. *J. Adv. Model. Earth Syst.* **8**, 1552–1564 (2016).
- Zhang, C. & Ling, J. Barrier effect of the Indo-Pacific Maritime continent on the MJO: Perspectives from tracking MJO precipitation. *J. Clim.* **30**, 3439–3459 (2017).

39. López-Romero, J. M. et al. Precipitation response to aerosol–radiation and aerosol–cloud interactions in regional climate simulations over Europe. *Atmos. Chem. Phys.* **21**, 415–430 (2021).
40. Boucher, O. et al. Clouds and aerosols. In: *Climate Change 2013: The Physical Science Basis. Contribution of Working Group I to the Fifth Assessment Report of the IPCC*. Cambridge University Press (2013).
41. Li, T. et al. A review of aerosol–cloud interactions: Mechanisms, climate effects, and challenges for modeling. *Atmos. Res.* **325**, 108267 (2025).
42. Tosca, M. G. et al. Do biomass burning aerosols intensify drought in equatorial Asia during El Niño?. *Atmos. Chem. Phys.* **10**, 3515–3528 (2010).
43. Liu, L. et al. Impact of biomass burning aerosols on radiation, clouds, and precipitation over the Amazon. *Atmos. Chem. Phys.* **20**, 13283–13301 (2020).
44. Iacono, M. J. et al. Radiative forcing by long-lived greenhouse gases: calculations with the AER radiative transfer models. *J. Geophys. Res.* **113**, D13103 (2008).
45. Mlawer, E. J., Taubman, S. J., Brown, P. D., Iacono, M. J. & Clough, S. A. Radiative transfer for inhomogeneous atmospheres: RRTM, a validated correlated-*k* model for the longwave. *J. Geophys. Res.* **102**, 16663–16682 (1997).
46. Morrison, H., Curry, J. A. & Khvorostyano, V. I. A new double-moment microphysics parameterization for application in cloud and climate models. *Part I: Descript. J. Atmos. Sci.* **62**, 1665–1677 (2005).
47. Morrison, H. & Pinto, J. O. Mesoscale modeling of springtime arctic mixed-phase clouds using a new two-moment bulk microphysics scheme. *J. Atmos. Sci.* **62**, 3683–3704 (2005).
48. Morrison, H. et al. Intercomparison of model simulations of mixed-phase clouds observed during the ARM Mixed-Phase Arctic Cloud Experiment. Part II: Multi-layer cloud. *Quart. J. Roy. Meteor. Soc.* **135**, 1003–1019 (2009).
49. Hong, S.-Y., Noh, Y. & Dudhia, J. A new vertical diffusion package with an explicit treatment of entrainment processes. *Mon. Weather Rev.* **134**, 2318–2341 (2006).
50. Dudhia, J. A multi-layer soil temperature model for MM5. Preprints, the sixth PSU/NCAR mesoscale model users’ workshop, 22–24 July 1995, Boulder, CO, 49–50 (1996).
51. Jiménez, P. et al. A revised scheme for the WRF surface layer formulation. *Mon. Weather Rev.* **140**, 898–918 (2012).
52. Chen, F. et al. The integrated WRF/urban modelling system: development, evaluation, and applications to urban environmental problems. *Int. J. Climatol.* **31**, 273–288 (2011).
53. Yoneyama, K., Zhang, C. & Long, C. N. Tracking pulses of the Madden–Julian oscillation. *Bull. Am. Meteor. Soc.* **94**, 1871–1891 (2013).
54. Zhang, C. et al. Cracking the MJO nut. *Geophys. Res. Lett.* **40**, 1223–1230 (2013).
55. Wheeler, M. & Hendon, H. H. An all-season real-time multivariate MJO index: Development of an index for monitoring and prediction. *Mon. Weather Rev.* **132**, 1917–1932 (2004).
56. Huffman, G. J. et al. The TRMM Multisatellite Precipitation Analysis (TMPA): Quasi-global, multiyear, combined-sensor precipitation estimates at fine scales. *J. Hydrometeorol.* **8**, 38–55 (2007).
57. Johnson, R. H. & Ciesielski, P. E. Structure and properties of Madden–Julian oscillations deduced from DYNAMO sounding arrays. *J. Atmos. Sci.* **70**, 3157–3179 (2013).
58. Ciesielski, P. E. et al. Quality-controlled upper-air sounding dataset for DYNAMO/CINDY/AMIE: development and corrections. *J. Atmos. Ocean. Technol.* **31**, 741–764 (2014).
59. Holben, B. N. et al. An emerging ground-based aerosol climatology: Aerosol optical depth from AERONET. *J. Geophys. Res.* **106**, 12067–12097 (2001).
60. Lee, S. S. et al. Aerosol as a potential factor to control the increasing torrential rain events in urban areas over the last decades. *Atmos. Chem. Phys.* **18**, 12531–12550 (2018).
61. Seinfeld, J. H. & Pandis, S. N. *Atmospheric Chemistry and Physics*, John Wiley & Sons, New York, 1326 (1998).

Acknowledgements

This study is supported by the Korea Meteorological Administration (KMA) Research and Development Program under Grant RS-2024-00403698 and Global Learning & Academic research institution for Master’s-PhD students, and Postdocs (LAMP) Program of the National Research Foundation of Korea (NRF) grant funded by the Ministry of Education (No. RS-2023-00301938). S.S.L. is supported by the National Research Foundation of Korea (NRF) grant funded by the Korea government (MSIT) (No. NRF2023R1A2C1002367). Ki-Hyun Nam assisted in plotting the cloud observation data.

Author contributions

K.-H.S. and S.S.L. conceived the essential ideas to initiate this paper and developed a detailed roadmap for data analysis and simulations. K.-H.S., J.C., and S.S.L. collected, scrutinized, and interpreted observed and simulated data. K.-H.S., J.C., S.S.L., and W.L. carried out a comprehensive review and refinement of the data analysis and interpretation, enhancing the depth and quality of this paper. All authors wrote the paper.

Competing interests

The authors declare no competing interests.

Additional information

Supplementary information The online version contains supplementary material available at <https://doi.org/10.1038/s41612-025-01215-5>.

Correspondence and requests for materials should be addressed to Kyong-Hwan Seo or Seoung Soo Lee.

Reprints and permissions information is available at <http://www.nature.com/reprints>

Publisher’s note Springer Nature remains neutral with regard to jurisdictional claims in published maps and institutional affiliations.

Open Access This article is licensed under a Creative Commons Attribution 4.0 International License, which permits use, sharing, adaptation, distribution and reproduction in any medium or format, as long as you give appropriate credit to the original author(s) and the source, provide a link to the Creative Commons licence, and indicate if changes were made. The images or other third party material in this article are included in the article’s Creative Commons licence, unless indicated otherwise in a credit line to the material. If material is not included in the article’s Creative Commons licence and your intended use is not permitted by statutory regulation or exceeds the permitted use, you will need to obtain permission directly from the copyright holder. To view a copy of this licence, visit <http://creativecommons.org/licenses/by/4.0/>.

© The Author(s) 2025